AIAA JOURNAL
Vol. 41, No. 4, April 2003

Computational Simulation of the Autonomous Navigation of a Biomimetic Underwater Vehicle

Samuel F. Galls* and Othon K. Rediniotis†
Texas A&M University, College Station, Texas 77843-3141

The computational work performed to navigate a biomimetic underwater vehicle autonomously is discussed. The navigation procedure uses as input a set of vehicle geometric and state variables, and from that it predicts the needed vehicle body deformations so that the vehicle can navigate through a set of given waypoints. The first task was to develop a two-dimensional numerical simulation based on an unsteady panel method coupled with the vehicle dynamics. Numerous test cases spanning the range of possible conditions were processed with the simulation, and these data were subsequently used to train a neural network. The trained network can predict what body deflection time history is necessary for the vehicle to navigate the given waypoints. Validation results are presented that show the accuracy of the present flow solver, and several test cases of autonomous navigation are presented to show the capabilities of the current method.

Nomenclature

A	=	amplitude of oscillation
a	=	cylinder diameter
C_p	=	pressure coefficient
C_x	=	force coefficient in the x direction
C_y	=	force coefficient in the y direction
c	=	chord
$\mathrm{d}t$	=	time step
F_x	=	X component of the resultant pressure force acting on the vehicle
F_y	=	Y component of the resultant pressure force acting on the vehicle
f, g	=	generic functions
h	=	height
i	=	time index during navigation
j	=	waypoint index
K	=	trailing-edge (TE) nondimensional angular deflection rate
k	=	time index in flow solver
N	=	number of panels
P	=	vehicle perimeter
$\boldsymbol{Q}$	=	velocity acting on each panel from the influence of the singularities
Q_n	=	normal flow velocity at panel centers
Q_t	=	tangential flow velocity at panel centers
q	=	dynamic pressure
$\boldsymbol{r}$	=	distance from center of rotation to panel center on vehicle
S	=	vehicle projected surface area
t	=	time
U_{ref}	=	reference velocity
U_w	=	X component of velocity on the wake element
V	=	vehicle velocity magnitude
$\boldsymbol{V}_c$	=	cylinder velocity
$\boldsymbol{V}_{\mathrm{surf}}$	=	surface velocity of the vehicle due to local deformations
$\boldsymbol{V}_0$	=	vehicle velocity vector in the inertial frame
W_w	=	Y component of velocity on the wake element
w_x, w_y	=	waypoint coordinates in the inertial frame
x, y	=	position of vehicle in inertial frame
Γ	=	circulation
γ_p	=	bound vortex strength
γ_w	=	wake element vortex strength
Δ	=	length of wake element
$\Delta T, \Delta T_2$	=	time steps defined in Fig. 7
$\Delta x, \Delta y$	=	relative x and y positions from the current vehicle frame of reference
$\Delta\theta$	=	change in body pitch
δ	=	angle from the center of the cylinder to the surface
θ	=	body pitch or rotation with respect to the x axis in the inertial frame
θ_{TE}	=	TE deflection with respect to the body centerline
σ	=	source strength
τ	=	nondimensional time, $t \cdot V/c$
Φ	=	total velocity potential
$\boldsymbol{\Omega}$	=	vehicle angular velocity

Received 19 February 2001; revision received 25 September 2001; accepted for publication 29 October 2002.

*Ph.D. Student, Aerospace Engineering Department. Associate Member AIAA.

†Associate Professor, Aerospace Engineering Department. Associate Fellow AIAA.

Introduction

THE development of highly maneuverable underwater vehicles is currently of interest, with their design being based on the undulatory body motion swimming techniques and anatomical structure of aquatic animals, primarily with respect to the highly controllable fins and the large aspect ratio lunate tail. This and similar pursuits in the field of air vehicles have triggered the emergence of the science of biomimetics, which is the study of natural systems to improve the design and functionality of synthetic systems.[1] Obviously, the tailoring and implementation of the accumulated knowledge into biomimetic vehicles is a task of multidisciplinary nature. The present work addresses the issue of overall vehicle navigation and control with the ultimate objective being the integration of vehicle dynamics and hydrodynamics control that can ultimately be implemented to constitute the control center of an autonomous biomimetic vehicle.

In earlier studies of fish motion, Lighthill[2] applied the slender-body theory of hydrodynamics to transverse oscillatory motions of slender fish, resulting in the elongated body theory. This study revealed the high propulsive efficiency of fish, a finding that alone renders the utilization of similar propulsive techniques in synthetic vehicles a very attractive quest. To pursue this idea, several studies have been conducted on the effect of fin appendages, the dynamics of slender fish, and the propulsion mechanisms of fish motion.[2–5] The propulsive investigations largely concentrated on the undulatory type of propulsion. Studies included analyses of a slender wing with passive chordwise flexibility,[6] two-dimensional potential flow

modeling over a thin waving plate of finite chord,[7–10] and two-dimensional flow modeling of flow over a waving plate of finite thickness.[11] Three-dimensional models have more recently been developed[12] utilizing both waving plate theory and comparisons of performance coefficients between fish and underwater vehicles.[13] Researchers have addressed the problem of the thrust-producing capability of moving hydrofoils.[14–18] This problem simulates the type of propulsion used by fish, which primarily involves the caudal, or tail, fin. The caudal fin of such animals produces thrust as it oscillates through the development of a reverse von Kármán vortex street that corresponds to a jetlike average velocity profile. However, such jets are convectively unstable, and there is only a narrow bandwidth of frequencies for which the von Kármán vortices and the jetlike profile coexist and for which the flow structure, that is, its form, is stable.[17] For frequencies in this bandwidth, optimal thrust efficiency is achieved.

In the field of artificial intelligence, a discipline emerged in the second half of the 20th century: artificial neural networks (ANN). Biological neural systems are not born preprogrammed with all of the knowledge and abilities that they will eventually have. A learning process takes place over time that modifies the biological network to encode new information. ANN simulate their biological counterparts. They simulate human and animal cognition and decision-making mechanisms and the processes for learning ("training"). Although it was not until recently that ANN received wide attention, its applications have only begun to be realized. Inspired by the architecture of cognitive systems in humans and animals, ANN provide a framework within which a machine can assimilate, in a comprehensive way, information collected during its interaction with its environment and learn how to respond effectively and efficiently to a diverse range of excitations.

The present work uses an unsteady potential flow solver to simulate the unsteady flow around a biomimetic hydrofoil and uses neural network techniques to develop the hydrofoil's navigation control. The motivation for the work was to develop the navigation control for a shape–memory–alloy (SMA) actuated biomimetic hydrofoil that we developed as part of an Office of Naval Research sponsored project. The objective of the navigation control algorithm is, based on the desired vehicle trajectory, to provide the necessary body deformations as input to the SMAs, which, in turn, by acting as muscles, achieve the commanded body deformation to navigate the vehicle through the desired trajectory.

Flow Solver: Computational Procedures

To provide a theoretical model of the two-dimensional fish motion, an unsteady potential panel code was developed. The general approach taken was similar to that used by Basu and Hancock,[19] properly modified to incorporate a body moving through fluid, as well as body deformations.[19] A schematic of the typical geometry is shown in Fig. 1. The hydrofoil surface is composed of N panels with source σ and vortex γ_p strengths. The source strengths vary from panel to panel, but constant vortex strength is assigned to all panels. A constant vortex panel attached to the trailing edge (TE) is used to model the wake shedding. The strength of this vortex wake panel is concentrated into a point vortex element that is shed into the flow at the end of each time step and allowed to convect with the local velocity. Vortex shedding was constrained to the TE only because the involved vehicle has a large profile with a blunt nose shape, where separation from the leading edge (LE) would be minimal if present.

The total number of unknowns at any given time step is $N + 3$: N source panel strengths σ_i, one vortex panel strength γ_p, the length of the vortex wake panel Δ_k, and the angle of the vortex wake panel θ_k. The condition of zero normal flow through the surface of the hydrofoil (the no-penetration condition) is used to provide N equations:

$$(Q_{nj})_k = 0 \tag{1}$$

where $(Q_{nj})_k$ is the total normal velocity at the control point of panel j at time t_k. The Kutta condition, which enforces zero loading at the TE of the hydrofoil, provides one additional equation:

$$(Q_{t1})_k^2 = (Q_{tN})_k^2 + \frac{2(\Gamma_k - \Gamma_{k-1})}{(t_k - t_{k-1})} \tag{2a}$$

which can be written in the form

$$\gamma_{pk} = \frac{(Q_{t1})_k^2 - (Q_{tN})_k^2}{2 \cdot P} \cdot \mathrm{d}t + 2 \cdot \Gamma_{k-1} \tag{2b}$$

using $\Gamma = \gamma_p \cdot P$ and for a constant time step of $\mathrm{d}t = t_k - t_{k-1}$. P is the perimeter of the body, that is, the summation of the panel lengths. In Eqs. (2a) and (2b), $(Q_{t1})_k$ and $(Q_{tN})_k$ are the total tangential velocities on panels 1 and N, respectively, at time t_k. Γ_k is the bound circulation on the hydrofoil at time t_k. The vortex wake panel length and angle are set by the condition that the element is tangential to the local flow and that its length is proportional to the resultant velocity. This provides the two final equations:

$$\tan(\theta_k) = (W_w)_k/(U_w)_k \tag{3}$$

$$\Delta_k = \left[(U_w)_k^2 + (W_w)_k^2\right]^{\frac{1}{2}}[t_k - t_{k-1}] \tag{4}$$

where $(U_w)_k$, $(W_w)_k$, and the total velocity components in the x and y directions, respectively, are induced on the midpoint of the vortex wake panel at time t_k. Because the preceding set of equations is nonlinear, an iterative process as suggested by Basu and Hancock[19] was used to find Δ_k and θ_k. This complete procedure is shown in Fig. 2. Note that there is a double iteration; the code needs to iterate fully on the bound circulation γ_p for every iteration of Δ_k and θ_k.

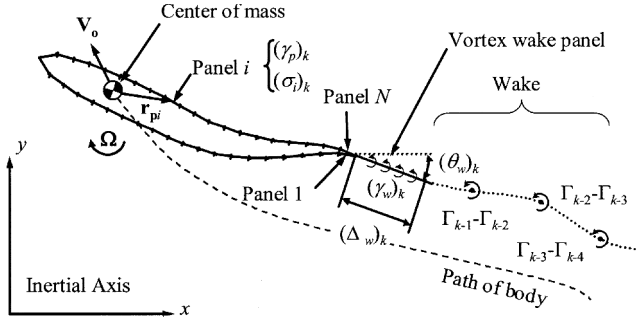

Fig. 1 Schematic of theoretical modeling of moving hydrofoil.

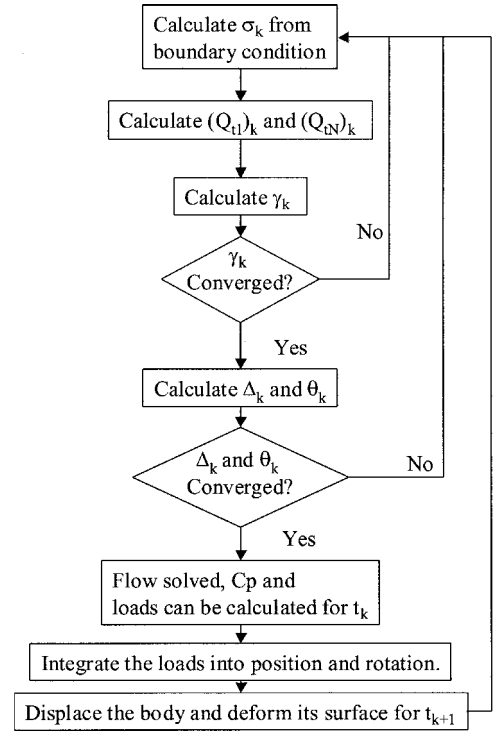

Fig. 2 Flowchart of flow solver computational procedure.

After the equations are solved for the $N + 3$ unknowns, the flow velocities on the body surface, as well as at each wake vortex location, are calculated as a superposition of the influences from the source panels, the bound vortex, and the vortices in the wake.[19] Once the flowfield has been solved for at a given time step, the surface pressures on the hydrofoil surface can be calculated. These pressures are calculated in terms of a nondimensional pressure coefficient that is found by use of the following equation for a moving body[20]:

$$C_P = -\frac{|\boldsymbol{Q}|^2}{U_{\text{ref}}^2} + \frac{2}{U_{\text{ref}}^2}[\boldsymbol{V}_0 + \boldsymbol{\Omega} \times r + V_{\text{surf}}] \cdot \boldsymbol{Q} - \frac{2}{U_{\text{ref}}^2}\frac{\partial \Phi}{\partial t} \qquad (5)$$

where $\boldsymbol{Q}$ is the flow velocity on the panel center due to the influence of the surface and wake singularity elements. $\boldsymbol{Q}$ is defined in the inertial coordinate system. The angular velocity of the body is given by $\boldsymbol{\Omega}$. The vector $\boldsymbol{r}$ is the distance from the rotation reference point to the panel, $\boldsymbol{V}_0$ is the velocity of the body as it travels trough the fluid, U_{ref} is an arbitrary reference velocity that is needed because there is no freestream in the inertial frame. The velocity $\boldsymbol{V}_{\text{surf}}$ is the velocity of the surface of the body due to local deformations such as body deflections. $\boldsymbol{V}_{\text{surf}}$ is calculated by second-order differencing of the panel centers using the coordinates of the last three body shapes. All of the vector quantities are given in the inertial frame of reference. The velocity potential on the panel was calculated by numerically integrating the velocity field from far upstream of the hydrofoil to the LE and then around the hydrofoil surface. Second-order backward differencing was used to estimate the time derivative of the velocity potential. Because the time derivative of the potential is needed, the starting point of integration was not important, as long as it was always the same and it was sufficiently far from the influence of the body.

After the solution has been obtained, the flowfield is then updated by convecting the discrete vortices in the wake and shedding a new discrete wake vortex from the vortex wake panel. At this point, the body surface is changed as needed. The last step in each iteration is to calculate the new position and pitch of the body. This position is relative to the inertial frame, and it is a direct result of the pressure distribution acting on the body. Body accelerations are directly derived from the loads. First-order Euler integration of the rotational and linear accelerations is used to obtain the angular and linear velocities for the next iteration. Finally, a second integration produces the current rotation and position of the body in the inertial frame. Higher-order explicit methods, such as the Adams–Bashford three-point integration, were tested. However, they did not provide any significant accuracy improvements and tended to be unstable in a few cases where load changes were relatively small or zero. The first-order Euler method proved to be very reliable and fairly insensitive to small load fluctuations produced by the discrete vortices introduced into the wake. Implicit methods were not used because it made the iterative part of the computational procedure intractable and increased the compute time by at least threefold.

Vehicle Geometry

To simulate the turning maneuvers similar to those that fish perform, continuously deformable boundaries were developed for the panel method. A typical shape for this case is shown in Fig. 3. The hydrofoil thickness distribution was that of a NACA 0012, whereas the hydrofoil camber was derived from a turning profile.[21] It was required for the panel code to simulate the hydrofoil as being made up of pivoting vertebrae. To achieve this, the body geometry was defined by a skeleton composed of rigid vertebrae that could rotate with respect to each other. The surface of the vehicle was created by fitting a skin over the skeleton. The skin is formed using a spline fit around the ends of the vertebrae. As the angles of the vertebrae change, the skin stretches or shrinks to conform to them. The panel code is general enough to accommodate any two-dimensional hydrofoil shape and motion. For the vehicle to perform a turn, it needs to flex its body. As shown in Fig. 3, the deflections of the vertebrae sections during a typical turn maneuver smoothly vary from zero to θ_{TE} between two points on the vehicle ($x1$–$x2$ in Fig. 3). The slope from the LE to $x1$ is zero, and from $x2$ to the TE the slope is $\tan(\theta_{\text{TE}})$. The smooth variation of slope between $x1$ and $x2$ is modeled using a fifth-order ramp. This model also included mass and inertia. These are needed in the integration of accelerations into displacements and rotations as the vehicle moves in the fluid.

Validation of the Flow Solver

A FORTRAN code incorporating the preceding computational procedure and geometry was developed on a Pentium II class desktop computer. To validate the accuracy of the present method, the panel code results were compared to an oscillating cylinder potential solution and a Navier–Stokes solution presented in Ref. 22. In the first test case, the cylinder was forced to move in the x direction at the following speed as a function of time:

$$V_c(t)/V_{c\,\max} = -[1 + 0.2 \cdot \sin(20\pi \cdot \tau)] \qquad (6)$$

In Eq. (6), $V_{c\,\max}$ is 30 diameters per unit time. The pressure coefficient for the exact potential solution was derived using a moving doublet and Eq. (5) and resulted in Eq. (7), where β is the angle around the cylinder as shown in Fig. 4:

$$Cp = \left(\frac{V_c}{V_{c\,\max}}\right)^2 - 4\left(\frac{V_c}{V_{c\,\max}}\right)^2 \sin^2(\beta) - \frac{1}{V_{c\,\max}^2}\frac{\mathrm{d}V_c}{\mathrm{d}\tau} a \cdot \cos(\beta) \qquad (7)$$

To calculate the pressure coefficient using the unsteady flow solver, the cylinder was modeled with 40 panels. It was moved in the x direction according to Eq. (6). Then these results were compared to the solution given by Eq. (7), and both are presented in Fig. 4. Note that the exact potential solution and the present method match very well. This is to be expected because the basis for both solutions are potential flow singularities. This also shows that the present code can handle rather large angles between the panels at

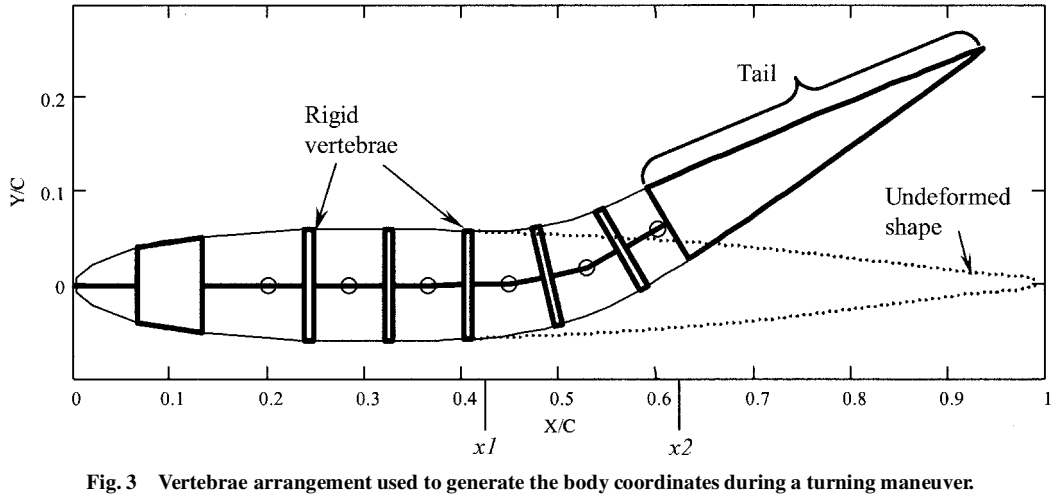

Fig. 3 Vertebrae arrangement used to generate the body coordinates during a turning maneuver.

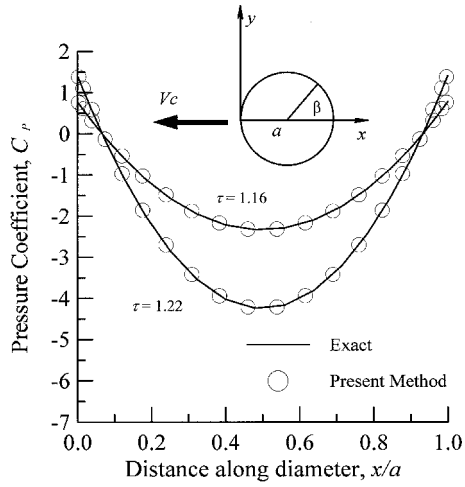

Fig. 4 Comparison of the pressure coefficient between the exact potential and the present method, for an oscillating cylinder.

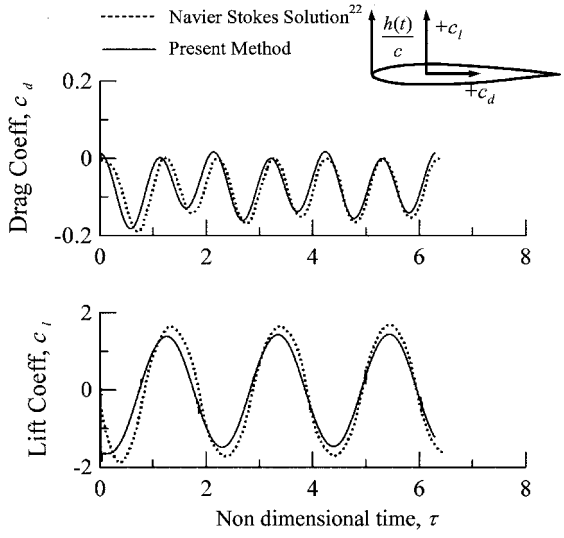

Fig. 5 Validation of the panel code with a Navier–Stokes solution of a plunging airfoil.

the TE, where the Kutta condition dictates that the pressure change across the wake should be zero.

The second test case was a comparison to a solution of the plunging motion of a rigid NACA 0012 profile[22] using the strong conservation form of the thin-layer Navier–Stokes equations. The Reynolds number in Ref. 22 was 3×10^6, and Mach number was 0.3. The plunging motion is given by Eq. (8), where the amplitude is $A = 0.1c$ and the reduced frequency is $k = 1.5$:

$$h/c = (A/c) \cdot \cos(2 \cdot k \cdot \tau) \tag{8}$$

The panel code used 120 panels to simulate the 120 grid points on the surface of the hydrofoil in the Navier–Stokes solution. The comparison of the resulting load coefficients is presented in Fig. 5. The agreement is good considering that the panel code does not take into consideration any viscous effects on the surface of the hydrofoil. Decreasing the resolution to 80 or 40 panels did not affect the solution significantly.

Formulation of Vehicle Control via Neural Networks

For the hydrofoil to navigate a given set of waypoints autonomously, a general relation among body deflections, flow conditions, vehicle motions, and desired trajectory must be determined. A neural network approach has been chosen for this purpose. The layout of the vehicle, as it travels a given path made up of waypoints, is given in Fig. 6. The path is formed by a cubic spline through the x and y coordinates of the waypoints. From this path description, the input variables can be preliminarily identified. The known

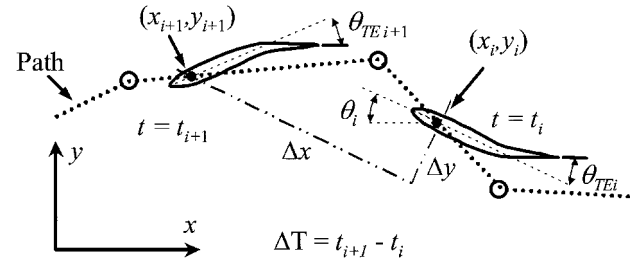

Fig. 6 Geometry description for vehicle during maneuvering.

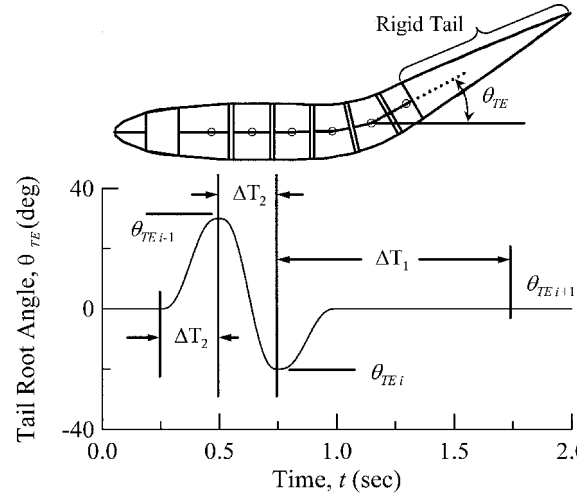

Fig. 7 TE motion used for the training cases.

information at time $t = t_i$ includes body pitch θ, TE angle deflection θ_{TE}, velocity magnitude V_i, and current vehicle position (x_i, y_i), along with the history of these variables at $t = t_{i-1}, t_{i-2}$, and earlier. The known information at $t = t_{i+1}$ is the desired vehicle position (x_{i+1}, y_{i+1}) at that time. All of the given waypoint positions (w_{xj}, w_{yj}) are also known. The vehicle will change direction by flexing its tail, so that at $t = t_i$, the only needed information is the amount that the TE should be deflected $(\theta_{\mathrm{TE}\,i+1} - \theta_{\mathrm{TE}\,i})$ so that the vehicle follows the path by reaching (x_{i+1}, y_{i+1}). The TE deflection $\theta_{\mathrm{TE}\,i+1}$ can, at most, depend on the following list of variables:

$$\theta_{\mathrm{TE}\,i+1} = g(x_{i+1}, x_i, x_{i-1}, \ldots, y_{i+1}, y_i, y_{i-1}, \ldots, V_i,$$

$$V_{i-1}, \ldots, \theta_{\mathrm{TE}\,i}, \theta_{\mathrm{TE}\,i-1}, \ldots, \theta_i, \theta_{i-1}, \ldots) \tag{9}$$

However, by the investigation of the effect of the input variables on the output variable $(\theta_{\mathrm{TE}\,i+1})$, significant order reduction can be achieved with negligible effect of the accuracy of the model. As we will see next, the total number of independent variables can be reduced to four. To this end, many training cases were executed using the panel code simulation described earlier. These cases were run by deflecting the TE through a range of different schedules. A typical TE deflection schedule is shown in Fig. 7. The deflection was varied between −30 and +30 deg, with each case being characterized by three distinct TE angle values: $\theta_{\mathrm{TE}\,i-1}$, $\theta_{\mathrm{TE}\,i}$, and $\theta_{\mathrm{TE}\,i+1}$. Each one of these angles was varied at 10-deg increments. For example, the hydrofoil would start undeformed at $t = 0$ s with a forward velocity of 1.0 m/s and then could be commanded to have a TE deflection of 10 deg at $t = 0.5$ s, then 20 deg at $t = 0.75$ s, and then −10 deg at $t = 1.0$ s. Then the vehicle state at $t = 1.75$ s is recorded and compiled into a list. Varying these angles in all possible combinations resulted in 154 unique test cases (the rest were discarded because of symmetry) that could be simulated using the panel code. For every case, the information in Eq. (9) was collected. The extended time delay after 1.0 s in Fig. 7 was added because, after a TE deflection, the vehicle will move in the opposite direction initially. This can be seen in Fig. 8. The vehicle, once the TE is deployed, experiences a downward force for a short time while the moment has not yet had time to rotate the vehicle. This results in a small vehicle displacement in the opposite direction of the TE deflection. A few moments later, the force changes direction, after the moment has had the time

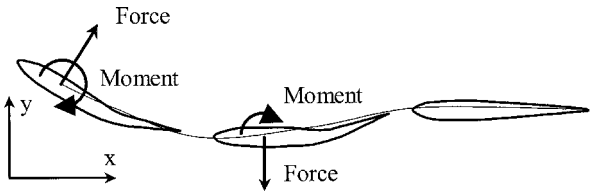

Fig. 8 Transient effect of TE deflection on the vehicle.

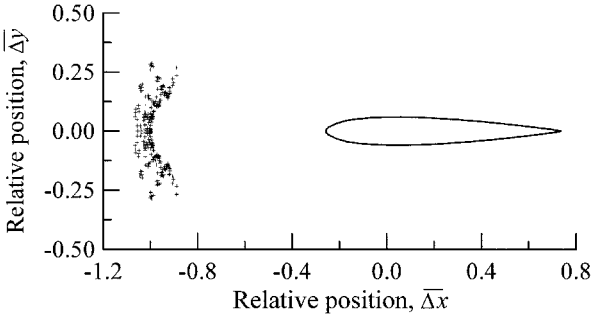

Fig. 9 Domain of (Δx, Δy) scaled and unscaled pairs resulting from training.

to make the vehicle turn in the desired direction. For a typical vehicle velocity of 1.0 m/s and the TE deflection rates considered here, it was found that it was necessary to add 0.75 s after the end of the TE deflection for the moment to develop and have a significant effect on the body rotation.

To be useful in this analysis, the final x and y positions of the vehicle after the TE deflection schedules were converted to nondimensional distances ($\overline{\Delta x}$, $\overline{\Delta y}$) relative to the current position of the vehicle and then transformed to the local vehicle axis, as seen in Fig. 6. The nondimensional positions reached after each TE deflection are given by Eqs. (10a) and (10b):

$$\overline{\Delta x} = \Delta x/(V \cdot \Delta T_1) \tag{10a}$$

$$\overline{\Delta y} = \Delta y/(V \cdot \Delta T_1) \tag{10b}$$

where V is the current vehicle velocity and ΔT_1 is 1.0 s from the training cases (Fig. 7). The domain of ($\overline{\Delta x}$, $\overline{\Delta y}$) pairs that resulted from the 154 test cases mentioned earlier is shown in Fig. 9. The time step corresponding to these ($\overline{\Delta x}$, $\overline{\Delta y}$) pairs was 0.0025 s. For these tests, 40 panels were used on the vehicle surface. By inspection of the distribution in Fig. 9, the number of variables in Eq. (9) can be reduced because the percentage variation of $\overline{\Delta x}$ is relatively small compared to that of $\overline{\Delta y}$. (As seen in Fig. 9, all $\overline{\Delta x}$ values are narrowly concentrated around -1.)

Because body pitch is the orientation of the vehicle in the inertial frame, a more insightful variable would be the relative pitch change from the earlier position to the current one:

$$\Delta\theta = \theta_i - \theta_{i-1} \tag{11}$$

Also, a way to include the history of the TE angle θ_{TE} is to define a variable that would capture the rate of TE angle deflection and scale it with the velocity and the chord of the vehicle. This quantity can be defined as

$$K = \frac{(\theta_{\mathrm{TE}\,i} - \theta_{\mathrm{TE}\,i-1}) \cdot c}{V \cdot \Delta T_2} \tag{12}$$

where the time interval ΔT_2 is fixed and is defined as shown in Fig. 7. Essentially, K is the nondimensional angular deflection rate of the TE. Given the preceding arguments, the TE angle at $t = t_{i+1}$ can be predicted using the simplified relation shown in Eq. (13):

$$\theta_{\mathrm{TE}\,i+1} = f(\theta_{\mathrm{TE}\,i}, K, \overline{\Delta y}, \Delta\theta) \tag{13}$$

This is a relation with four inputs and one output, and it can be easily trained in a neural network setup. The current network model is shown in Fig. 10. This model uses a feedforward network, trained through backpropagation. The first and second layers use a

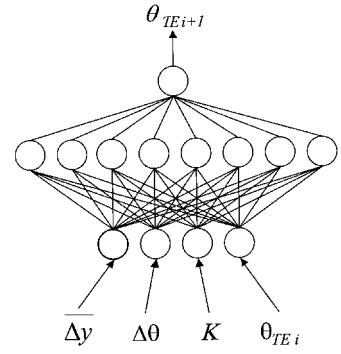

Fig. 10 Neural network layout used for navigation.

hyperbolic tangent sigmoid transfer function. The last layer uses a linear transfer function. It was discovered that more layers, nodes per layer, or data from points older than $t = t_{i-1}$ did not improve prediction accuracy. The trained network could model the TE angle history with an accuracy of better than 1 deg.

To test the accuracy of the navigation algorithm, the following procedure was used:

1) At the ith time instant, calculate the distance $\Delta x = V \cdot \Delta T$ that the vehicle will cover with the current velocity during a time lapse of ΔT.

2) On the path (formed by the waypoints), determine the point that, in the body reference frame, has an x coordinate equal to Δx.

3) Set Δy equal to the y coordinate (in the vehicle's reference axes) of the point identified in step 2.

4) Scale Δy into $\overline{\Delta y}$ using the current velocity V and ΔT. Also, calculate the other input variables from the current and earlier conditions.

5) Feed the input variables to the trained neural network. The network output $\theta_{\mathrm{TE}\,i+1}$ is the predicted TE deflection, at the text time step $i+1$, necessary to navigate the vehicle to the trajectory point identified in step 2.

6) Calculate the exact position of the vehicle at the $i+1$ instant by using the panel method simulation to solve up to $t = t_{i+1}$. The difference between this exact position and the trajectory point identified in step 2 is a measure of the navigation algorithm accuracy.

7) Advance the time instant and return to step 1.

It was found that, if the preceding procedure is performed at intervals of ΔT_1 seconds (1.0 s as shown in Fig. 7), the prediction was accurate, but the vehicle would oscillate about the path. Sampling the path at a faster rate, such as ΔT_2 in Fig. 7, can alleviate this overshoot. The sampling can be anything from ΔT_2 to ΔT_1. The quantities ΔT_1 and ΔT_2 are dependent on how the test cases were executed. In the present method, as indicated in Fig. 7, $\Delta T_1 = 1.0$ s and $\Delta T_2 = 0.25$ s. Note that the waypoints are used only to produce the path. Once this is done, the present procedure will interpolate, according to current velocity and sampling, to generate the intermediate path points.

As expected, the mass and inertia of the vehicle do affect its behavior during a TE maneuver. Larger mass values made the velocity magnitude and direction of the vehicle very insensitive to changes in body shape or TE deflection. Likewise, as the mass was decreased, the velocity of the vehicle became very responsive to body deformations, to the point of almost being unstable during the simulation. Similarly, increasing and decreasing the inertia of the vehicle decreased and increased correspondingly the rotational velocity sensitivity to body deformations. As the inertia was decreased, the turning radius of the vehicle, while the TE was locked into a fixed deflection, was also decreased. Locating the center of mass was also critical to the performance of the vehicle. Placing the center of mass too close to the LE resulted in the vehicle being very stable and requiring large deflections for proper control. If the center of mass is located toward the TE of the body, the vehicle will become unstable, especially if it is located behind its aerodynamic center. The goal was to set a realistic mass, center of mass, and inertia that will provide a maneuverable vehicle without making it too unstable. The model mass chosen was 10.0 kg, with a center of mass at 12% of the chord from the LE, and the inertia used was $0.5\ \mathrm{N \cdot m \cdot s^2}$.

Error Estimates

To evaluate the navigation technique's error, we first estimated the uncertainty in the ANN training, that is, how accurately the ANN predicts the data with which it was trained. This effectively is given by the sum-squared difference between the ANN output and the desired output for the training data. This was calculated for all of the training cases and was found to be 0.5%. However, the latter uncertainty does not necessarily apply to cases where the ANN is asked to operate on data/trajectories for which it was not trained. To address this uncertainty, we have performed quantitative estimates of the vehicle deviation from a new, heretofore unknown, prescribed path (for which the ANN was not specifically trained), as a function of the path curvature and vehicle velocity. For these tests, the vehicle was started at a constant velocity and was asked to navigate autonomously a circular path, 20 body lengths ($20c$) long. Several different cases were run, with the arc radius R varying from $2c$ to $32c$, and the velocity was varied from 1.2 body lengths per unit time ($1.2V/c$) to around 2.2 ($2.2V/c$). The error in navigation was determined by calculating the perpendicular distance from the vehicle (the origin of body-fixed reference frame) to the desired trajectory during navigation.

A sample trajectory error is shown in Fig. 11a. This is for the case with $R/c = 16$ and V/c (average during navigation) of about 1.2. The maximum position error is about 6% and the rms error for this case was 3.7%. The oscillations present in Fig. 11a indicate the correction cycles from the navigation scheme. Note that the error is diminished every $\Delta t\, V/c = 0.25$. This corresponds to the time lapse between trajectory searches/sampling used in the navigation of the vehicle. Once the vehicle corrects its path by deflecting the tail to the angle dictated by the navigation, it gets closer to the desired path. However, because no further control action is taken until the next trajectory search/sampling, the vehicle might start to diverge. At the next trajectory search, the vehicle would then correct again, and the cycle is repeated.

Figure 11b shows the position uncertainty of the navigation technique, as a function of path radius and vehicle velocity. (The velocity shown is the average velocity of the vehicle during the navigation along the arc.) The error presented in Fig. 11b is the rms error normalized by the body length c. As seen in Fig. 11b, larger vehicle velocities and smaller path radii increase the navigation error. For a large turning radius, the error is relatively unaffected by velocity and ranges from 2 to 9% of body length. Cases with a larger turning radius would typically yield position errors as small as 1%. As the turning radius is decreased, the vehicle navigation must compensate more to follow the trajectory that is "seen" ahead by the vehicle and that it is more likely to overshoot, thus leading to larger navigation errors.

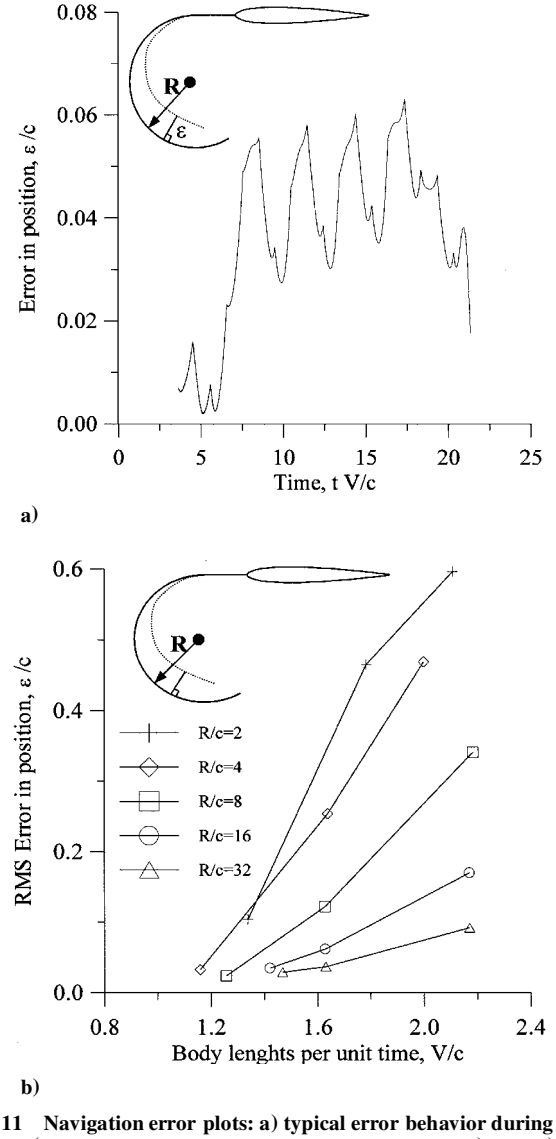

Fig. 11 Navigation error plots: a) typical error behavior during navigation (the case presented is for $R/c = 16$ and $V/c = 1.2$) and b) rms navigation error as a function of path radius and vehicle velocity.

Results from Sample Navigation Cases

All of the sample navigation cases were performed with the flow solver using a time step of $dt = 0.0025$ s and 40 panels on the vehicle surface. The procedure outlined in the preceding section, along with the panel code, was used to trace given waypoints. All of the cases described here used a vehicle with a chord length of 0.612 m. All simulations start at $(x, y) = (0, 0)$ with an initial velocity of 1.0 m/s (or 1.63 chords/s) in the direction of negative x. Thus, the objective is not to propel the vehicle, but to navigate it through the waypoints, under the influence of the initial vehicle velocity. All trajectory plots are normalized by the chord of the vehicle. Given that the surrounding fluid in the cases being simulated is water, the representative Reynolds number would be about 7×10^5. The first case shown in Fig. 12 is a random set of waypoints. In this case, the effects of using different trajectory sampling times can be seen. For a larger sampling time ($\Delta T_1 = 1.0$ s), the navigation follows the path but the oscillations make it impractical. Decreasing the sampling time to $\Delta T_1 = 0.25$ s improves the navigation dramatically by eliminating unwanted oscillations. Figure 12 also shows successful navigation for three different initial velocities. This shows that the scaling allows the present method to be applied to conditions not trained for and indicates that the network is applicable in most operating cases through scaling. The sampling time for this and the rest of the navigation examples is $\Delta T_1 = 0.25$ s. The range of rotational speeds of the tail of the vehicle is from 0 to 240 deg/s.

The second case shows the vehicle navigating around a square in Fig. 13. This simulation shows the overshoot and navigation stability. The overshoot is present due to the limiting turning radius that the vehicle has, with a maximum TE deflection of ±30 deg. The starting and final vehicle shapes are also shown in Fig. 13. A similar navigation example (third case) is shown in Fig. 14, where more

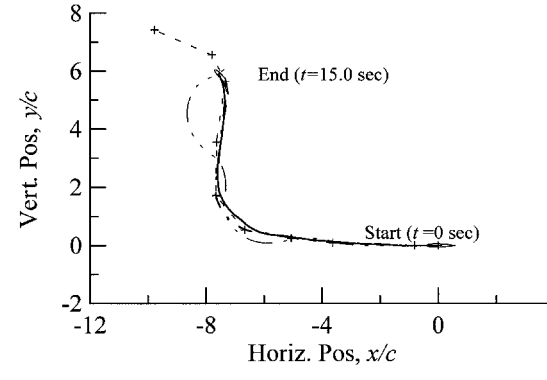

Fig. 12 Sample navigation case 1 with different sampling times and starting velocities: +, waypoint path; ——, vehicle trajectory, $V = 1.5$ m/s, and $\Delta T = 0.25$ s; – – –, vehicle trajectory, $V = 1.0$ m/s, and $\Delta T = 1.0$ s; and – · –, vehicle trajectory, $V = 0.5$ m/s, and $\Delta T = 0.25$ s.

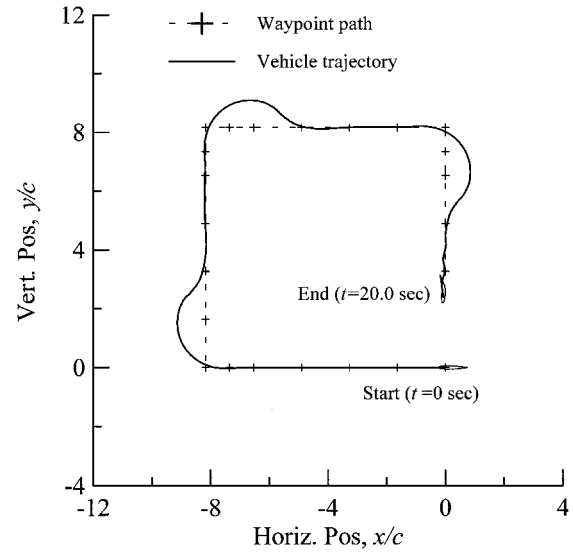

Fig. 13 Sample navigation case 2.

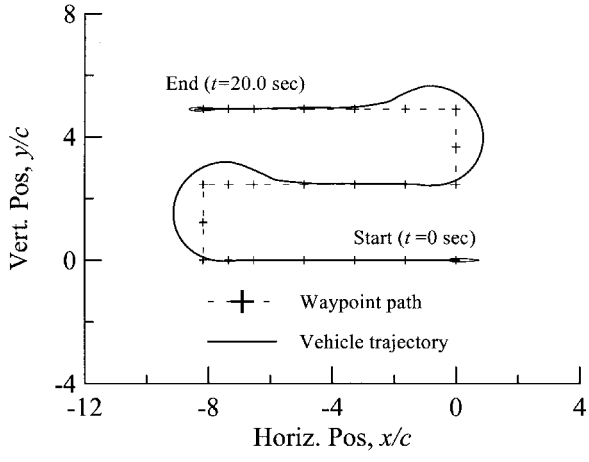

Fig. 14 Sample navigation case 3.

abrupt maneuvering was needed to stay on course. The tests shown in Figs. 13 and 14 also show that the present method can sustain the vehicle on a straight path accurately. The overshoot and turning radius of the vehicle could be improved by changing the location of the center of gravity and by changing the body deflections used for the turns.

Conclusions

The navigation procedure for a biomimetic underwater vehicle was simulated using an unsteady flow solver with vehicle dynamics and a neural network. The unsteady panel method was used to generate the data so that the most important parameters could be identified. By incorporation of the vehicle dynamics into the unsteady flow solver, the resulting vehicle positions due to numerous deflection inputs were calculated. The generated data were studied, and the important geometric and flow variables were identified and properly scaled. This allowed us to achieve significant model order reduction. Subsequently, the reduced data were used to train the neural network. The network input was a set of geometric and state variables, and it could predict the needed body deformations so that the vehicle could navigate through a set of given waypoints. Validation results showed that the present method could handle various trajectories from sharp cornering to maintaining straight trajectories. Our initial trajectory sampling resulted in unwanted vehicle oscillations about the path. These oscillations were eliminated by faster path sampling. The test cases also show that the present method can be scaled to different vehicle velocities not covered during training.

Acknowledgments

This work was supported by the Office of Naval Research and Aeroprobe, Inc., through the Small Business Technology Transfer program, under Contract N00014-98-C-0061. The authors thank the Technical Monitor of the project, Teresa McMullen, for her support.

References

[1] *On-line Medical Dictionary* [online], Academic Medical Publishing and CancerWEB, URL: http://www.graylab.ac.uk/cgi-bin/omd?biomimetics, 1998.

[2] Lighthill, M. J., "Note on the Swimming of Slender Fish," *Journal of Fluid Mechanics*, Vol. 9, 1960, pp. 305–317.

[3] Lighthill, M. J., "Aquatic Animal Propulsion of High Hydrodynamical Efficiency," *Journal of Fluid Mechanics*, Vol. 44, No. 2, 1970, pp. 265–301.

[4] Newman, J. M., and Wu, T. Y., "A Generalized Slender Body Theory for Fish-Like Forms," *Journal of Fluid Mechanics*, Vol. 57, No. 4, 1973, pp. 673–693.

[5] Karpouzian, G., Spedding, G., and Cheng, H. K., "Lunate-Tail Swimming Propulsion, Part 2. Performance Analysis," *Journal of Fluid Mechanics*, Vol. 210, No. 4, 1990, pp. 329–351.

[6] Katz, J., and Weihs, D., "Hydrodynamic Propulsion by Large Amplitude Oscillation of an Airfoil with Chordwise Flexibility," *Journal of Fluid Mechanics*, Vol. 88, No. 3, 1978, pp. 485–497.

[7] Wu, T. Y., "Swimming of a Waving Plate," *Journal of Fluid Mechanics*, Vol. 10, 1961, pp. 321–344.

[8] Wu, T. Y., "Hydromechanics of Swimming Propulsion, Part 1. Swimming of a Two-Dimensional Flexible Plate at Variable Forward Speeds in an Inviscid Fluid," *Journal of Fluid Mechanics*, Vol. 46, No. 2, 1971, pp. 337–355.

[9] Siekmann, J., "Theoretical Studies of Sea Animal Locomotion, Part I," *Ingenieur-Archiv*, Vol. 31, 1962, pp. 214–228.

[10] Siekmann, J., "Theoretical Studies of Sea Animal Locomotion, Part 2," *Ingenieur-Archiv*, Vol. 32, 1963, pp. 40–50.

[11] Uldrick, J. P., and Siekmann, J., "On the Swimming of a Flexible Plate of Arbitrary Finite Thickness," *Journal of Fluid Mechanics*, Vol. 20, 1964, pp. 1–33.

[12] Cheng, J. Y., Zhuang, L. X., and Tong, B. G., "Analysis of Swimming Three-Dimensional Waving Plates," *Journal of Fluid Mechanics*, Vol. 232, 1991, pp. 341–355.

[13] Bandyopadhyay, P. R., Rice, J. Q., Corriveau, P. J., and Macy, W. K., "Maneuvering Hydrodynamics of Fish and Small Underwater Vehicles, Including the Concept of an Agile Underwater Vehicle," Naval Undersea Warfare Center Div., NUWC-NPT TR 10,494, Newport, RI, 1995.

[14] Isshiki, H., and Murakami, M., "A Theory of Wave Devouring Propulsion," *Journal of the Society of Naval Architects of Japan*, Vol. 156, 1984, pp. 102–114.

[15] Koochesfahani, M., "Vortical Patterns in the Wake of an Oscillating Airfoil," *AIAA Journal*, Vol. 27, No. 9, 1989, pp. 1200–1205.

[16] Triantafyllou, G. S., Triantafyllou, M. S., and Gopalkrishnan, R., "Wake Mechanics for Thrust Generation in Oscillating Foils," *Physics of Fluids*, Vol. 3, No. 12, 1991, pp. 2835–2837.

[17] Triantafyllou, G. S., Triantafyllou, M. S., and Grosenbaugh, M. A., "Optimal Thrust Development in Oscillating Foils with Application to Fish Propulsion," *Journal of Fluids and Structures*, Vol. 7, No. 2, 1993, pp. 205–224.

[18] Nakashima, M., and Ono, K., "Numerical and Experimental Study of the Propulsive Speed of the Three Joint Bending Propulsion Mechanism," College of Engineering, Tokyo Inst. of Technology, Tokyo, May 1995.

[19] Basu, B. C., and Hancock, G. J., "The Unsteady Motion of a Two-Dimensional Aerofoil in Incompressible Inviscid Flow," *Journal of Fluid Mechanics*, Vol. 87, No. 1, 1978, pp. 159–178.

[20] Katz, J., and Plotkin, A., *Low-Speed Aerodynamics*, McGraw–Hill, New York, 1991, pp. 421–511.

[21] Blake, R. W., *Fish Locomotion*, Cambridge Univ. Press, Cambridge, England, U.K., 1983, pp. 85–123.

[22] Tuncer, I. H., and Platzer, M. F., "Thrust Generation due to Airfoil Flapping," *AIAA Journal*, Vol. 34, No. 2, 1994, pp. 324–331.

P. R. Bandyopadhyay
Associate Editor